Journal of Materials Chemistry B

ROYAL SOCIETY OF CHEMISTRY

PAPER

View Article Online
View Journal | View Issue

Cite this: *J. Mater. Chem. B*, 2024, **12**, 6203

Silk–gelatin hybrid hydrogel: a potential carrier for RNA therapeutics

Binapani Mahaling,† Chandrashish Roy† and Sourabh Ghosh *

Received 7th March 2024,
Accepted 18th May 2024

DOI: 10.1039/d4tb00491d

rsc.li/materials-b

RNA-based therapeutics have exhibited remarkable potential in targeting genetic factors for disease intervention, exemplified by recent mRNA vaccines for COVID-19. Nevertheless, the intrinsic instability of RNA and challenges related to its translational efficiency remain significant obstacles to the development of RNA as therapeutics. This study introduces an innovative RNA delivery approach using a silk fibroin (SF) and positively charged gelatin (Gel) hydrogel matrix to enhance RNA stability for controlled release. As a proof of concept, whole-cell RNA was incorporated into the hydrogel to enhance interactions with RNA molecules. Additionally, molecular modeling studies were conducted to explore the interactions between SF, collagen, chitosan (Chi), and the various RNA species including ribosomal RNAs (28S, 18S, 8.5S, and 5S rRNAs), transfer RNAs (tRNA-ALA, tRNA-GLN, and tRNA-Leu), as well as messenger RNAs (mRNA-GAPDH, mRNA-β actin, and mRNA-Nanog), shedding light on the RNA–polymer interaction and RNA stability; SF exhibits a more robust interaction with RNA compared to collagen/gel and chitosan. We confirmed the molecular interactions of SF and RNA by FTIR and Raman spectroscopy, which were further supported by AFM and contact angle measurement. This research introduces a novel RNA delivery platform and insights into biopolymer–RNA interactions, paving the way for tailored RNA delivery systems in therapeutics and biomedical applications.

Introduction

Ribonucleic acid (RNA) is involved in various biological processes, including gene regulation, protein synthesis, the transfer of genetic information, and catalyzing biochemical reactions. RNA molecules, such as messenger RNA (mRNA), small interfering RNA (siRNA), microRNA (miRNA), and antisense oligonucleotides (ASOs), have gained significant attention in the field of therapeutics.[1–5] However, delivering RNA molecules to target cells can be challenging due to their vulnerability to degradation and difficulty in crossing cellular barriers.[6] There are several methods for RNA delivery, such as lipid-based delivery, viral vectors, electroporation, nanoparticles, and hydrogels, but the choice of method depends on the specific RNA molecule, target cells, and intended therapeutic application.[4,7] The local delivery of RNA hydrogel provides unique advantages over other systems because of their potential to be injectable, localize, control, and sustain delivery of high levels of payloads while maintaining the biological activity of RNA.[4,5]

Hydrogels have garnered significant attention for RNA delivery due to their characteristics, such as biodegradability, tunable physicochemical properties, injectability, and stimuli-responsive properties.[4,5,8–10] Silk fibroin (SF) and gelatin (Gel) are frequently employed natural biomaterials for hydrogel generation, thanks to their favorable mechanical, chemical, and biological properties.[11] SF–Gel hydrogels ensure minimal adverse reactions when interacting with cells and tissues.[12] The SF–Gel hydrogel structure can be precisely engineered in terms of geometry, the number or thickness of coatings, and porosity to control the release rate of RNA and injectability, enabling sustained delivery over an extended period and stimuli-responsive drug delivery properties.[9,10,13,14] The polymer characteristics, including molecular mass and crystallinity/β-sheet content, can be controlled to govern the release kinetics.[14] The utilization of a cationic charge is common in such hydrogels because of its potent electrostatic interactions, which play a significant role in influencing the release of RNA. In contrast, neutral hydrogels are electrostatically inert and do not engage in direct interactions with charged nucleic acids. On the other hand, anionic hydrogels facilitate a swift release.[15] SF imparts high mechanical strength and shows slow enzymatic degradation, while Gel incorporates bioactive motifs that contribute to biomimicry in the resulting biomaterial.[16,17] SF undergoes degradation both *in vitro* and *in vivo* in the presence of proteolytic enzymes such as protease XIV, α-chymotrypsin, proteinase K, papain, collagenase, and others, however, these enzymes do not have adverse effects on the encapsulated RNA.[18] By tailoring

Regenerative Engineering Laboratory, Department of Textile and Fibre Engineering, Indian Institute of Technology Delhi, New Delhi, 110016, India.
E-mail: sourabh.ghosh@textile.iitd.ac.in; Tel: +91-11-2659-1440
† Both the authors have contributed equally.

the mechanical and physical properties of SF–Gel hydrogels, such as stiffness and porosity, the optimal conditions for RNA delivery can be achieved.[16,19] SF is known for its ability to stabilize encapsulated RNA, preventing rapid oxidation, while Gel's amphoteric nature allows for high encapsulation efficiency of RNA.[20,21] Moreover, silk possesses a low isoelectric point (PI), enabling it to maintain conformational stability even at neutral pH and in the presence of buffer salts.[20,22] The release of RNA from gels is primarily facilitated by diffusion and degradation mechanisms. RNA molecules are initially encapsulated within the gel matrix, where they are held by interactions such as electrostatic forces and hydrogen bonding. Over time, RNA molecules diffuse out of the gel matrix or are released due to the degradation of the gel structure. Environmental factors such as pH and temperature can influence the release kinetics. The SF–Gel hydrogel matrix acts as a protective shield, safeguarding RNA molecules from degradation caused by enzymes or harsh environmental conditions. The entrapped mRNA in the SF–Gel hydrogel matrix is prone to RNase activity, which leads to RNA degradation through enzymatic means, supported by ribonucleases (RNases). RNases may break down mRNA because of its single-stranded structure and exposed ribonucleotides. Protective measures like the SF–Gel hydrogel matrix are necessary to protect RNA molecules because despite the hydrogel matrix's stability, it might not be able to completely prevent mRNA from enzymatic degradation. Chitosan (Chi) is a naturally occurring polysaccharide that has gained significant attention in biomedical applications due to its biodegradability, and low toxicity. Chi nanoparticles have been extensively investigated as carriers for nucleic acids, including RNA, in gene delivery systems.[23] Therefore, in this study we used Chi hydrogel as a control.

In the present study, the main goal was to develop SF and Gel-based hydrogels for an RNA delivery system. We used a positively charged Gel for hydrogel fabrication to enhance the stability of the RNA. As a principle of concept, we used whole-cell RNA for the controlled release study. We performed molecular modelling of SF, collagen, and chitosan with RNA (including 28S, 18S, 8.5S, and 5SrRNA; tRNA-ALA, tRNA-GLN, and tRNA-Leu; mRNA-GAPDH, mRNA-β actin, and mRNA-Nanog) to predict the interactions. The experimental and *in silico* data show that SF exhibits stronger interactions with RNA than collagen/Gel and chitosan.

Results and discussion

Release kinetics and stability of RNA analyzed by agarose gel electrophoresis

The SF–Gel and RNA-loaded SF–Gel thin film were cast from 150 μL of SF–Gel or 420 ng RNA per 150 μL SF–Gel solution in 24 well-plate sterile cell culture plates. The release kinetics was performed on days 1, 2, and 3 and the cumulative release kinetics was plotted. The observed release was higher than the loaded RNA (Fig. 1A). To assess the effectiveness of an RNA delivery system and the interactions of RNA with SF and Gel we conducted gel electrophoresis to evaluate the integrity of RNA loaded on thin films. In the agarose electrophoresis analysis, we observed that the control RNA exhibited no fluorescence at the well, indicating the absence of DNA contamination. Four distinct bands were clearly visible in the control RNA (Fig. 1B). However, we consistently observed fluorescence at the well across all time points when we examined the released RNA. The absence of fluorescence at the well in the control RNA sample suggested no DNA contamination. Fluorescence observed in released RNA samples may indicate interaction with the gel matrix. Further investigation showed RNA forming complexes with SF and gelatin, suggesting a stabilizing effect. This supports the idea that the fluorescence in released RNA samples is due to RNA–hydrogel matrix interactions rather than DNA contamination. This observation suggests that the RNA interacted with the thin film composed of SF and gelatin, preventing its separation during gel electrophoresis. To investigate the stabilizing effect of Gel, SF, or SF + Gel on RNA, we incubated the RNA with these three groups. We found that SF alone and combined with gelatin formed a complex with the RNA. This was evidenced by the presence of a fluorescence band at the well for both SF and SF–Gel, whereas no such band was observed for gelatin alone (Fig. 1C). The change in zeta

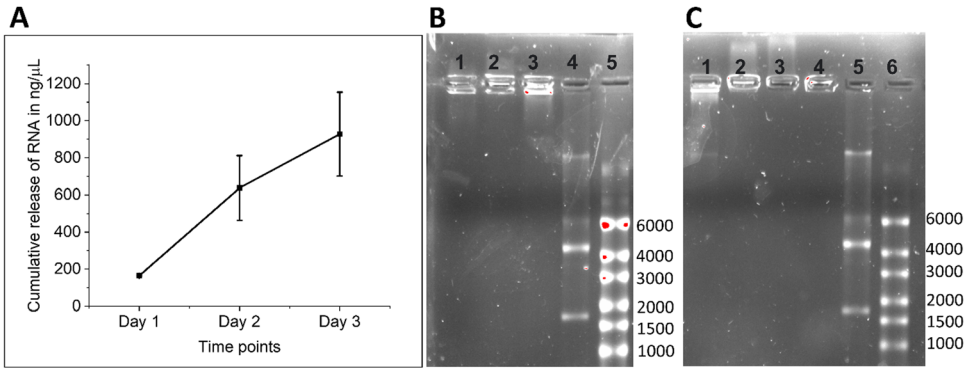

Fig. 1 Release kinetics and agarose gel electrophoresis for RNA. (A) Release kinetics of RNA from SF–Gel hydrogel; the original load of RNA was 420 ng/150 μL. (B) Agarose gel electrophoresis of total RNA released on day 1 (lane-1), day 2 (lane-2), and day 3 (lane-3), control RNA (lane-4) and RNA ladder (lane-5). (C) Gel electrophoresis to study interactions of RNA with chitosan (lane-1), SF (lane-2), Gel (lane-3) and SF + Gel (lane-4), control RNA (lane-5), and ladder (lane-6).

potential after RNA and SF incubation both indicated the formation of an RNA–SF complex (Fig. 3). This was further predicted by molecular modeling (Fig. 5) and confirmed by FTIR analysis. Additionally, AFM surface structural changes (Fig. 6–9) and contact angle measurements (Fig. 10) supported the existence of this complex.

The effective protection and delivery of RNA molecules are crucial for the success of RNA-based therapies. Hydrogels offer desirable properties such as biodegradability, tunable physicochemical characteristics, and injectability, making them attractive candidates for RNA delivery.[4,8] The mechanical properties of the hydrogel can be tailored to meet specific requirements, such as gel stiffness and porosity, for optimal RNA delivery.[16,19] The interactions between RNA and the hydrogel components were carefully examined. The agarose gel electrophoresis data indicated that Gel alone demonstrated limited protection for RNA, highlighting the need for further modifications. The unbound carboxyl groups on Gel were neutralized by incorporating tyramine, thereby establishing a positively charged environment, attributed to the remaining free amino groups on the Gel structure. This modification significantly improved the affinity of Gel for RNA and provided a positively charged Gel matrix for RNA stabilization.[21,24] SF showed slow enzymatic degradation of the hydrogel and played a crucial role in stabilizing the encapsulated RNA, shielding it from rapid oxidation.[20] SF possesses a hydrophobic nature and high glass-transition temperature, which contribute to its thermodynamic stability against temperature and moisture variations. The mechanical strength and toughness of silk stem from the extensively interconnected β-sheet structures, allowing it to effectively stabilize RNA molecules.[20,25]

Tyramine modification for gelatin and Gel–TA hydrogel fabrication

Gelatin is suitable for RNA delivery due to its endocytic properties. The agarose electrophoresis data revealed that Gel alone was not providing complete protection for RNA. To enhance the protection and delivery of negatively charged mRNA, we employed a modification strategy where the free carboxyl groups present in gelatin were neutralized by the amino groups on tyramine molecules. Tyramine conjugation was achieved by employing a carbodiimide crosslinking reaction that linked the amino group of tyramine with the carboxyl group of gelatins *via* the formation of amide bonds. This process led to an overall reduction in the quantity of negatively charged carboxyl groups present on the gelatin.[24,26] The tyramine modification level achieved was determined to be 0.443 ± 0.005 mM. Gel demonstrated a negative zeta potential, while Gel–TA exhibited a positive zeta potential, indicating successful tyramine modification (Fig. 2A). To ensure stable hydrogel formation, we standardized the concentrations of HRP and H_2O_2. It was observed that gelation occurred within a fraction of a second. The use of 2 or 3 units of HRP was found to be suitable for stable thin film formation (Fig. 2B). Similarly, a H_2O_2 concentration of 2 or 3 mM provided a stable thin film (Fig. 2C). High concentrations of H_2O_2 could not effectively facilitate hydrogel formation because they led to the rapid and excessive generation of free radicals, which in turn caused uncontrolled polymerization reactions.

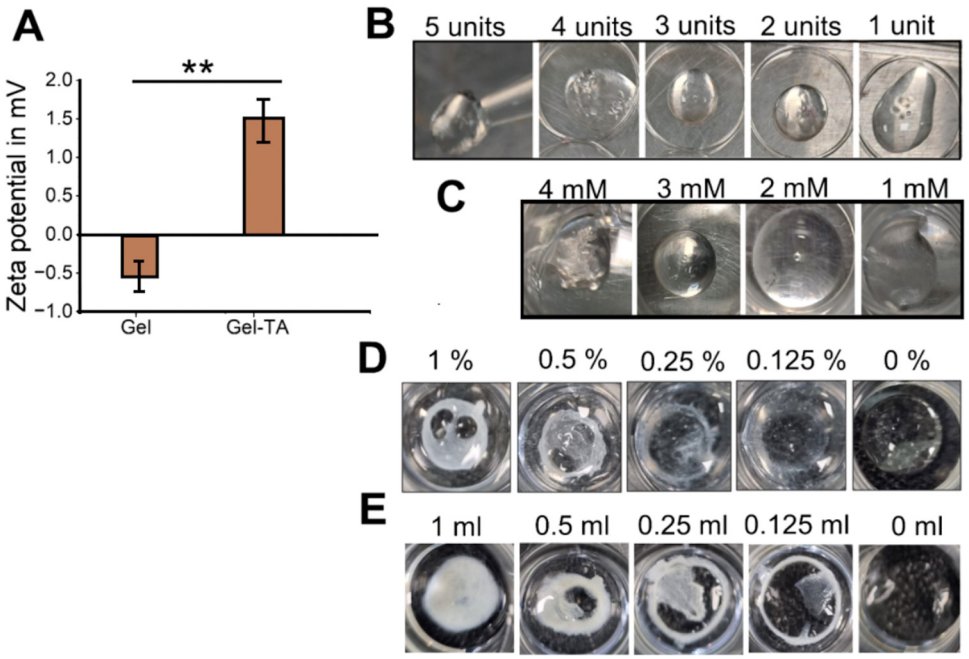

Fig. 2 Standardization of Gel–TA and chitosan thin film fabrication. (A) Zeta potential of Gel and Gel–TA for tyramine modification. (B) The effect of concentration of HRP on Gel–TA thin film formation. (C) The effect of H_2O_2 concentration on Gel–TA thin film formation. (D) and (E) Standardization of TPP concentration and volume for homogeneous stable chitosan thin film formation. All the results are presented as mean ± SD, **($p < 0.01$), $n = 3$.

This modification resulted in the creation of a positively charged environment, primarily contributed by the remaining free amino groups on the Gel. By "wiping out" the free carboxyl groups and introducing positive charges through the tyramine modification, we aimed to improve the efficacy of RNA protection and delivery. This approach capitalizes on the electrostatic interactions between the positively charged Gel and the negatively charged mRNA, potentially enhancing the stability and delivery efficiency of the mRNA.[24] The absorbance analysis at 260 nm demonstrated that the RNA interacted with the polymer matrix, resulting in an increase in absorbance in the supernatant compared to the initially loaded RNA. This interaction further confirmed the successful binding of RNA to the hydrogel system as RNA molecules possess purine and pyrimidine rings with conjugated double bonds, exhibiting a distinct absorption peak at 260 nm.

Chitosan hydrogel fabrication for RNA delivery

Chi, a polymer with a high cationic potential, is well-known for its ability to protect RNA from degradation during transport, as well as its remarkable transfection efficiency.[27–30] Chitosan-based hydrogel thin films were made using TPP as a cross-linker. When a TPP solution is added to dilute Chi solutions, the anions quickly cross-link the cationic Chi chains, forming nanoparticles or aggregates.[31] By carefully controlling the TPP concentration and volume, we could fine-tune the reaction rate and cross-linking density, thereby optimizing the properties of the stable, homogeneous chitosan-based hydrogel thin films. To ensure the desired properties of the polymeric network and the fabrication of stable thin films, we standardized the concentration and volume of TPP used in the reaction. We observed that lower concentrations of TPP led to the formation of nanogels, while higher concentrations resulted in the formation of stable thin films (Fig. 2D). This finding emphasizes the significance of controlling the TPP concentration to achieve the desired film morphology and stability. In addition to the TPP concentration, the volume of TPP utilized also played a crucial role in the formation of chitosan thin films. Insufficient TPP volume was found to be inadequate for effective cross-linking and thin film formation, whereas a higher volume (1 mL) facilitated the homogeneous formation of thin chitosan films (Fig. 2E).

When Chi interacts with RNA, several processes occur. One key interaction is electrostatic binding, driven by the positive charge of chitosan and the negative charge of RNA. RNA molecules typically carry a negative charge due to the presence of phosphate groups in their structure. The electrostatic interaction between the positively charged Chi and the negatively charged RNA enables the formation of chitosan–RNA complexes. The reduction in zeta potential occurs due to the neutralization of the positive charge of chitosan by the negatively charged RNA. As chitosan binds to RNA, the positive charge on Chi is distributed over a larger surface area, leading to a decrease in the overall surface charge. The electrostatic binding between RNA and cationic polymers can be influenced by factors such as polymer molecular weight, charge density, the proportion of protonatable polymer amine groups to nucleic acid phosphate groups, and the ionic strength of the

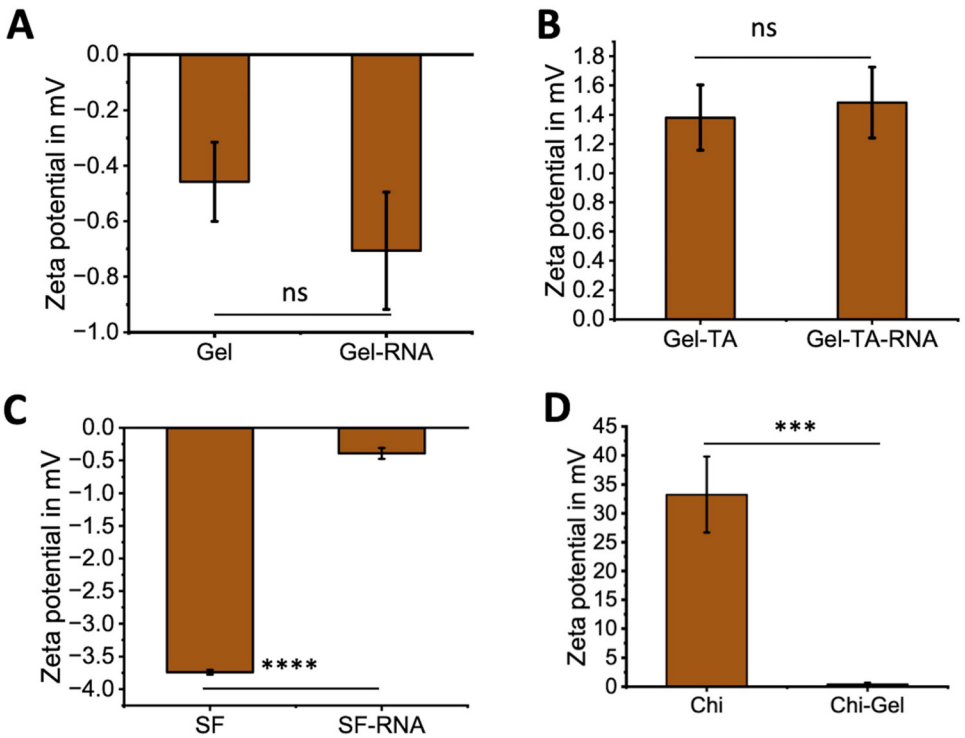

Fig. 3 Polymer and RNA interactions studied by zeta potential measurement. (A) Interaction between Gel and RNA. (B) Interaction between Gel–TA and RNA. (C) Interaction between SF and RNA, and (D) interaction between Chi and RNA. All the results are presented as mean ± SD. ***($p < 0.001$), $n = 3$.

surrounding medium.[32] This interaction is crucial for the stability and condensation of RNA within Chi carriers, protecting the RNA from degradation and facilitating its cellular uptake. This reduction in zeta potential indicates the formation of Chi–RNA complexes.[33]

RNA and polymer interaction

A prerequisite for effective RNA carriers is their ability to interact with RNA. The interaction between RNA and polymer is important for the successful delivery of RNA from the construct to the cell or tissue. The interaction between RNA and positively charged gel is stronger as compared to negatively charged gelatin.[21] Upon interaction with RNA, the Gel exhibits a slightly more negative zeta potential, possibly due to increased exposure of carboxyl groups (–COOH), although the difference is not significant (Fig. 3A). Conversely, Gel–TA did not significantly affect the surface charge (Fig. 3B). The alterations in zeta potential resulting from the Gel–RNA interactions can impact the stability and behavior of gelatin-based hydrogels used for RNA delivery. The interaction between SF and RNA was highly significant, as evident from the gel electrophoresis and zeta potential data (Fig. 1B and 3C). The increase in zeta potential from −3.5 to −0.4 indicates the exposure of more amino (NH_2) groups on the outer surface of the SF–RNA complex. These changes in zeta potential can affect the stability of SF–Gel hydrogels and the behavior of the encapsulated RNA

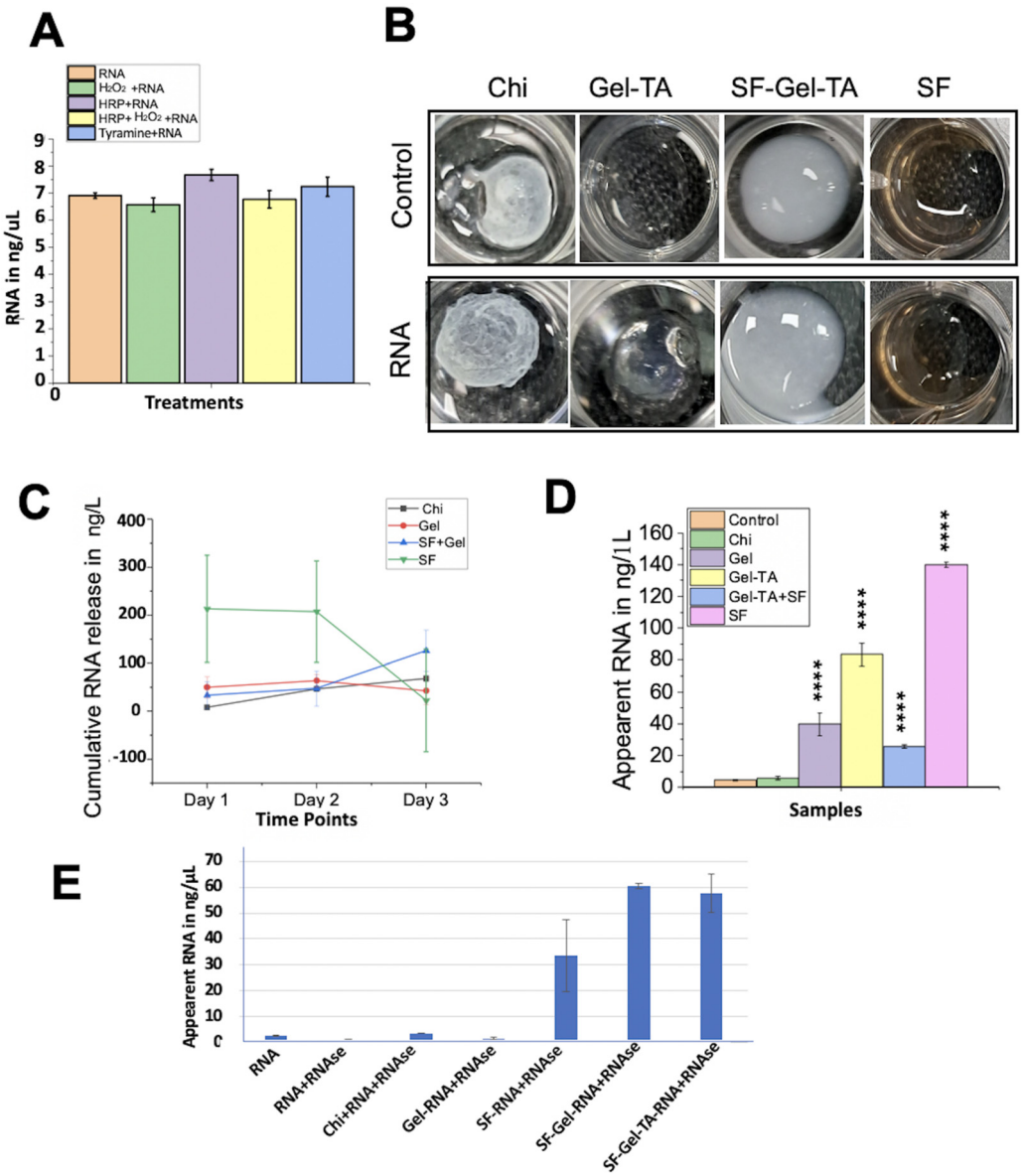

Fig. 4 RNA-loaded hydrogel fabrication, and the release kinetics of RNA. (A) The effects of H_2O_2, HRP, and tyrosinase on RNA stability. (B) Morphology and control and RNA-loaded hydrogels. (C) Release kinetics of RNA from the hydrogel. (D) Apparent RNA concentration as compared to the actual RNA used for RNA–polymer interaction. (E) The protection of RNA in the presence of gel from RNAse treatment. All the results are presented as mean ± SD, ****($p < 0.0001$), $n = 3$.

molecules. However, the zeta potential of Chi–RNA showed the reverse trend, where the surface charge of Chi was higher than that of Chi–RNA (Fig. 3D).

Stability of RNA

Before loading RNA with hydrogel, the stability of RNA in the presence of H_2O_2, HRP, and tyrosinase on RNA was evaluated and no degradation of RNA was observed (Fig. 4A). Upon loading RNA into the hydrogel, there were no significant changes in the morphology of the hydrogel across all experimental groups (Fig. 4B). Analysis of the supernatant collected at different time points revealed a substantially higher RNA content as compared to the initially loaded RNA. The RNA interacted with the polymer, leading to an increase in absorbance at 260 nm (Fig. 4C). This was further confirmed by the increase in apparent RNA as compared to the actual RNA (4 ng μL^{-1}) (Fig. 4D).

The successful delivery of RNA therapeutics hinges on preserving RNA integrity in the presence of RNAse, an enzyme that can rapidly degrade RNA molecules. We assessed the potential of SF, SF–Gel, (SF–Gel–TA), and Chi as a control for stabilizing RNA against RNAse degradation. By incubating a mixture of RNA and various polymers (Chi/Gel/SF/SF–Gel, SF–GelTA) in the presence of RNAse, we evaluated the protective effects of these polymers on RNA stability. Chi, SF, SF–Gel, and SF–GelTA were capable of shielding RNA from RNAse-mediated degradation. However, Gel alone did not exhibit the same protective effect (Fig. 4E). These findings highlight the specific contributions of SF and SF–Gel–TA in conferring protection against RNAse activity. The observed inability of Gel alone to safeguard RNA suggests that the combination of SF with Gel and tyramine modification on Gel is crucial for achieving effective RNA stabilization. Furthermore, our results corroborate previous observations, reinforcing the reliability and consistency of our findings. This consistency across

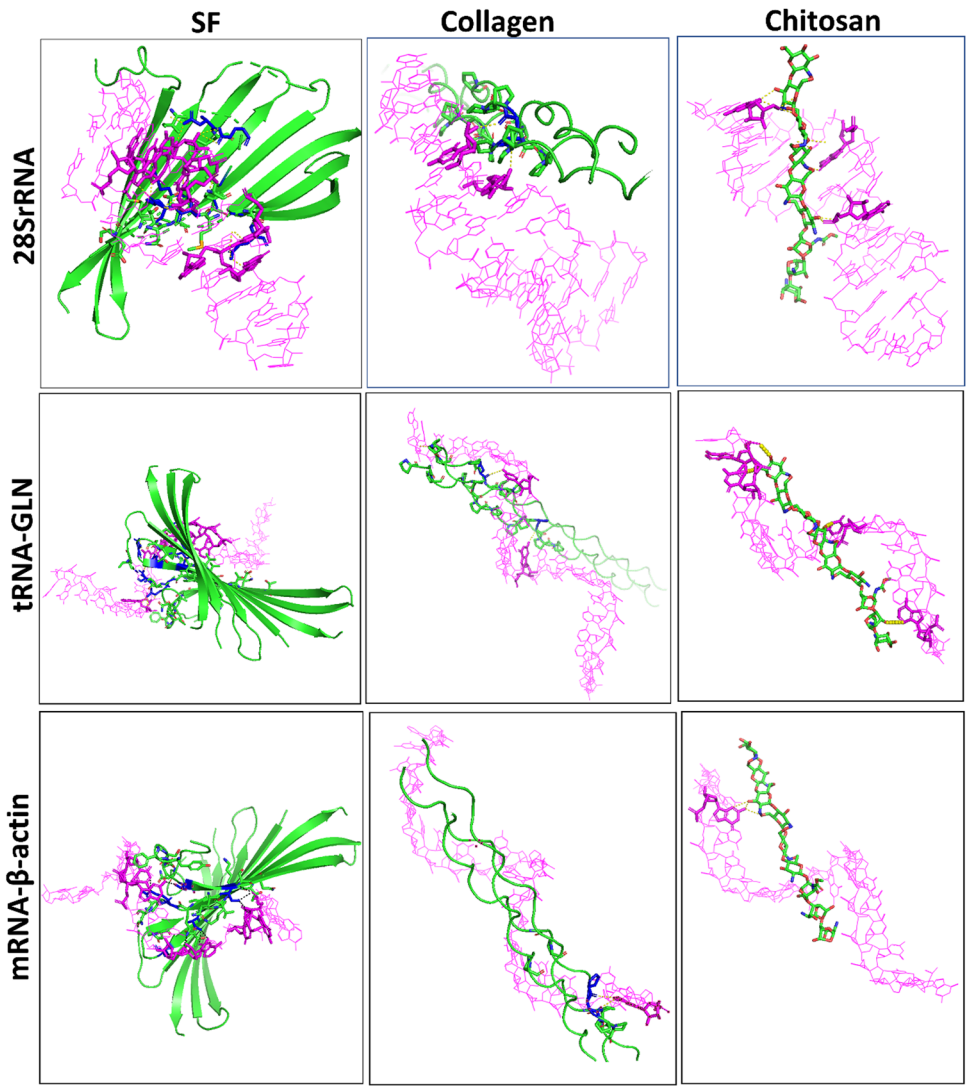

Fig. 5 Molecular modeling of the N-terminal sequence of fibroin (SF), collagen triple helix, and chitosan with 28S rRNA, tRNA-ALA, and mRNA-β-actin. SF, collagen, and chitosan are used as receptors, and 28S rRNA, tRNA-GLN, and mRNA-β-actin are used as ligands. The blue color represents interacting amino acids with nucleotides (represented as sticks) from RNA and the yellow dotted line represents the hydrogen bond.

experiments lends additional support to the robustness of our methodology and the validity of the results.

Molecular modeling of polymer RNA interaction

SF and Chi interacted with the RNA at the groove, whereas collagen interacted at the unintended site of the RNA. SF showed more hydrogen bonds as compared to the Chi, followed by collagen (Fig. 5).

The root mean square deviation (RMSD) values further supported these observations. SF–RNA interactions generally displayed lower RMSD values compared to collagen–RNA interactions, with the exception of 5.8SrRNA, tRNA-ALA, and mRNA-Nanog, where RNA–collagen interactions had lower RMSD values than RNA–Chi (as shown in Table 1). These findings suggest that SF has a stronger affinity for RNA compared to both collagen and chitosan in most cases, which is also substantiated by the greater number of hydrogen bonds formed between SF–RNA compared to Chi–RNA and collagen–RNA (Table 2). This enhanced interaction is consistent with both experimental and computational data. Our results also demonstrated that rRNA and tRNA generally exhibited stronger interactions with the biomolecules than mRNA, as evidenced by lower RMSD values, except for 18SrRNA, which showed comparable interactions. This pattern was consistent with the number of hydrogen bonds formed between the receptors (SF, collagen, and chitosan) and their respective RNA targets (Table 2).

Common residues from SF and RNA involving hydrogen bonding include ASP25 (SF)–U4 (RNA), 28GLU (SF)–G7 (RNA), 36THR (SF)–G7, and G24 (RNA). In the case of collagen, these interactions include 18Gly (chain A)–20A (RNA), and 18Gly (chain B)–13C (RNA). On the other hand, chitosan–RNA interactions feature residues like 1A, 21A, and 24G (RNA). In the context of 18SrRNA, the interaction between SF and RNA exhibits lower binding affinity compared to collagen. The specific interacting components in this case involve 38GLN (SF) and 40A (RNA). In contrast, collagen shows interactions with 18SrRNA through 5Pro (chain C)–1069U (RNA), 1Pro (chain C)–1065A (RNA), and 1Pro (chain B)–1065A (RNA).

Chitosan interacts with residue 358G of RNA. The 5.8SrRNA has stronger interaction with SF as compared to collagen and chitosan. The interacting components are 33Ser (SF)–63U (RNA), 34Asp (SF)–64G (RNA). 39Ser (SF)–63U, 64G, 54A (RNA) and 65Gln (SF)–58A (RNA). Collagen shows interactions with 5.8SrRNA through 18Gly (chain F)–86C (RNA) and Chi with 74A of RNA. 5SrRNA forms more hydrogen bonds with SF followed by chitosan, however, collagen does not exhibit any hydrogen bond with 5SrRNA (Table 2).

For all three simulated tRNA, the number of hydrogen bonds formed between SF and RNA was higher than the chitosan and collagen (Table 2). Hydrogen bonds were formed between tRNA-GLN and SF, 87THR (SF)–U13, 12G (RNA), 95SER (SF)–14A, 13U (RNA), ASN39 (SF)–G12, 11U (RNA), 68ASN (SF)–10G (RNA), 91 ASP (SF)–10G (RNA), and 66ARG (SF)–7A (RNA). Collagen forms hydrogen bonds between 5Pro (chain A)–44C (RNA) and 11Pro (chain A)–50G (RNA), whereas, Chi forms hydrogen bonds with 23C, 24A, 32C, and 38A of RNA. Similarly, tRNA-Leu forms hydrogen bonds with the following residues of SF and RNA, 61THR-54G, SER39-54G, 95SER-51A, 87THR-50C, 93ASN-49G, 66ARG-44G, and 66ARG-43G. Collagen forms hydrogen bonds between 17Pro (chain F)–61G (RNA) and 18Gly (chain F)–16G (RNA) and Chi with 50A of RNA. The interacting components of tRNA-ALA and SF are 33Ser 36THR-56G, 26PHE-59C, 66ARG-55A, Gly32-55A, 30TYR-56G, 31PHE-56G, and 56GLN-47XNA. Collagen interacted with tRNA-ALA through 5Pro (chain D)–29G and chitosan with 67C and 72C of RNA.

SF formed more hydrogen bonds when tRNA was conjugated, as compared to chitosan and collagen (Table 2). Shared residues between SF and mRNA-GAPDH that participate in hydrogen bonding interactions comprise 30TYR-479A, 26PHE-C480, 36THR-487C, 36THR-477C, and 66ARG-476A. In the case of collagen, the interaction was between 18Gly (chain A) and 52C. Chitosan interacts with 287C, 288C, and 289A nucleotides of mRNA-GAPDH. Common residues from SF and mRNA-β actin involving hydrogen bonding include 39SER-749G, 39SER-795C, 95SER-797A, 89ASP-789XNA, 66ARG-802C, and 36THR-80G. In the case of collagen, these interactions include 23Pro (chain E)–G1227 and 24Gly (chain E)–G1227. Chitosan–RNA interacts with the mRNA-β actin at 201G. Similarly, mRNA-Nanog forms hydrogen bonds with the following residues of SF and RNA, 41ASN-472A, 43THR-47G, T43HR-470A, and 28GLU-466XNA. Collagen forms hydrogen bonds between 5Pro (chain F)–56C and chitosan with 485-XNA, 486-G, and 499-G nucleotides of RNA. SF, collagen, and Chi were employed as receptors, while RNA molecules (including 28S, 18S, 8.5S, and 5SrRNA; tRNA-ALA, tRNA-GLN, and tRNA-Leu; mRNA-GAPDH, mRNA-βactin, and mRNA-Nanog) served as ligands. A molecular modeling study was conducted to investigate the interactions between receptors and ligands. Since the binding selectivity is largely influenced by the presence of directional hydrogen-bonding groups on the receptor surface, it complimented the ligand's hydrogen-bonding potential. This hydrogen bonding imparts a crucial directionality and specificity to the interaction, constituting a fundamental aspect of molecular recognition.[34] SF shows a higher number of hydrogen bonds than the Chi and collagen, except in 18SrRNA. Receptor–ligand complex formation was governed by the geometric and electrostatic compatibility between the interacting regions of the molecules.

Table 1 RMSD values for polymer–RNA interactions

Types of RNA	RNA	Silk fibroin	Collagen	Chitosan
rRNA	28SrRNA	32.51	83.07	51.56
	18SrRNA	3808.2	1814.14	3873.60
	5.8SrRNA	190.76	254.58	291.06
	5SrRNA	100.97	279.30	275.32
tRNA	tRNA-GLN	92.79	213.87	122.27
	tRNA-LEU	146.15	150.80	182.74
	tRNA-ALA	161.04	121.69	154.37
mRNA	mRNA-GAPDH	2790.38	2444.93	1116.64
	mRNA-β actin	2599.25	2957.60	2404.77
	mRNA-Nanog	1603.37	1818.45	1877.53

Table 2 Receptor and ligand interactions. SF, collagen, and Chi are used as receptors, and RNAs as ligands

Types of RNA	RNA	Silk fibroin	Collagen	Chitosan
rRNA	28SrRNA	25ASP-U4	18Gly (chain A)–20A	1A
		28GLU-G7	18Gly (chain B)–13C	21A
		36THR-G7, G24		24G
		38GLN-9G		
		65GLN-G7		
		66Arg-U7, C8, C24		
		82Lys-G3		
	18SrRNA	38GLN-40A	5Pro (chain C)–1069U	358G
			1Pro (chain C)–1065A	
			1Pro (chain B)–1065A	
	5.8SrRNA	33Ser-63U	18Gly (chain F)–86C	74A
		34Asp-64G		
		39Ser-63U, 64G, 54A		
		65Gln-58A		
	5SrRNA	39SER-55A	No hydrogen bond	74A
		65GLN-58A		
		65GLN-57C		
		66ARG-64G		
		66ARG, 34ASP, 35SER-63A		
tRNA	tRNA-GLN	87THR-U-13, 12G	5Pro (chain A)–44C	23C
				24A
		95SER-14A, 13U	11Pro (chain A)–50G	32C
		ASN39-G12, 11U		38A
		68ASN-10G		
		91ASP-10G		
		66ARG-7A		
	tRNA-LEU	61THR-54G	17Pro (chain F)–61G	50A
		SER39-54G	18Gly (chain F)–16G	
		95-SER-51-A		
		87THR-50-C		
		93ASN-49-G		
		66-ARG-44G		
		66-ARG-43G		
	tRNA-ALA	36THR-56G	5Pro (chain D)–29G	67C
		26PHE-59C		
		66ARG-55A		72C
		Gly32-55A		
		30TYR-56G		
		31PHE-56G		
		56GLN-47XNA		
mRNA	mRNA-GAPDH	30TYR-479A	18Gly (chain A)–52C	287C
				288C
		26PHE-C480		289A
		36THR-487C		
		36THR-477C		
		66ARG-476A		
	mRNA-βactin	39SER-749G	23Pro (chain E)–G1227	201G
		39SER-795C	24Gly (chain E)–G1227	
		95SER-797A		
		89ASP-789XNA		
		66ARG-802C		
		36THR-80G		
	mRNA-Nanog	41ASN-472A	5Pro (chain F)–56C	485-XNA
				486-G
		43THR-47G		499-G
		T43HR-470A		
		28GLU-466XNA		

The fulfillment of hydrogen bond donors and acceptors within the binding site significantly contributes to the energetic stability of receptor–ligand complexes.[34] Notably, proline's distinctive feature is its role in extending polypeptide structures, while glycine is the sole amino acid with an exceptionally small side group (–H), facilitating unhindered hydrogen bonding between the peptide group and external molecules.[35] Chitosan primarily establishes hydrogen bonds with guanine, cytosine, and adenine within RNA molecules. These intermolecular interactions rely on the formation of donor–acceptor hydrogen bond pairs between Chi and RNA. Specifically, hydrogen atoms attached to the nitrogen atoms of RNA bases, the oxygen atoms within the ribose sugar, and Chi serve as donors, while the phosphate groups within RNA act as receptors.[36] When examining the RMSD values, rRNA and tRNA demonstrate more robust interactions with SF, collagen, and chitosan compared to mRNA.[37,38]

AFM

AFM analysis of SF, SF–RNA, and RNA films revealed notable morphological distinctions. The AFM images in Fig. 6A–C depict the typical roughness of a pristine SF film at the submicrometric scale, characterized by grains of a few nanometers. In contrast, Fig. 6D–F illustrates the AFM image of RNA, showcasing larger grains with a more clustered structure. Upon incubation with PBS, an increase in grain size was observed over time, evolving into non-uniform crescent-shaped structures with higher porosity (Fig. 6G–L). This comparative analysis highlights significant morphological variations among the examined groups. The 3D structure of AFM images clearly illustrates the uniformity of grains in SF, each with a peak height of 3 nm (Fig. 7A–C). In contrast, RNA exhibits non-uniform grains with a larger size and a peak height of 12 nm (Fig. 7D–F). The grain size further increases in SF–RNA after incubation in PBS. Notably, the non-uniformity of grain size intensifies with prolonged incubation time, as shown in Fig. 7G–L. Specifically, at 1 hour and 6 hours, the grain peak heights measure 14 μm and 23 nm, respectively. From the depth histogram data, it was indicated that in SF, RNA, SF–RNA 1 h, and SF–RNA 6 h the maximum percentage of grain height ranges from 10–20, 300–400, 40–50, and 5–35 nm, respectively. These results indicate that RNA drastically changed the surface roughness of SF at the nanometer scale (Fig. 8).

To assess surface roughness, three parameters were considered: RMS roughness (R_q), which represents the root mean square average of profile heights over the evaluation length; roughness average (R_a), which indicates the arithmetic average

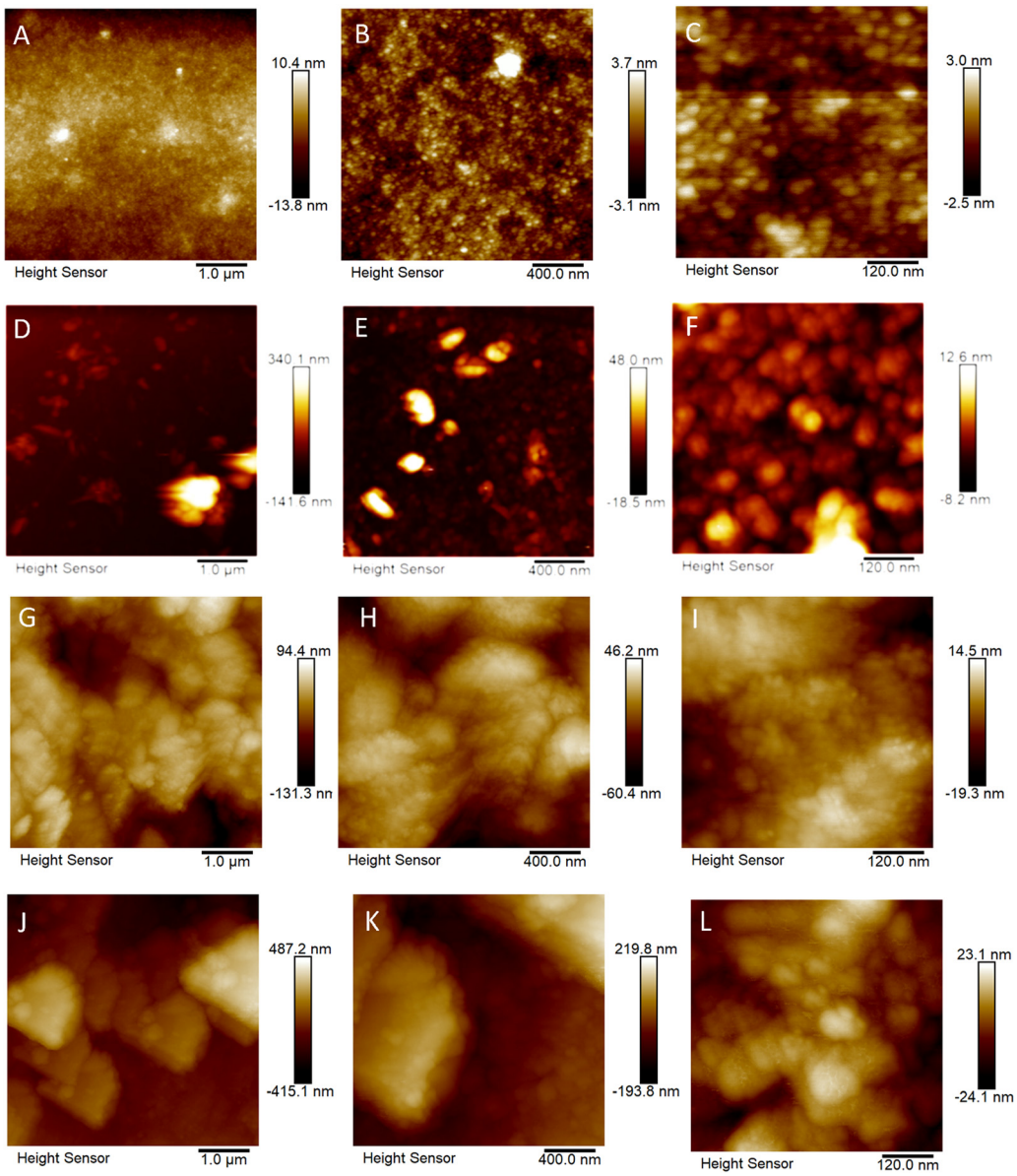

Fig. 6 2D AFM images of SF. (A)–(C) RNA (D)–(F) SF–RNA 1 h (G)–(I) and SF–RNA 6 h (J)–(L). For the first column, the scale bar is 1 μm; the second column, 400 nm, and the third column, 120 nm.

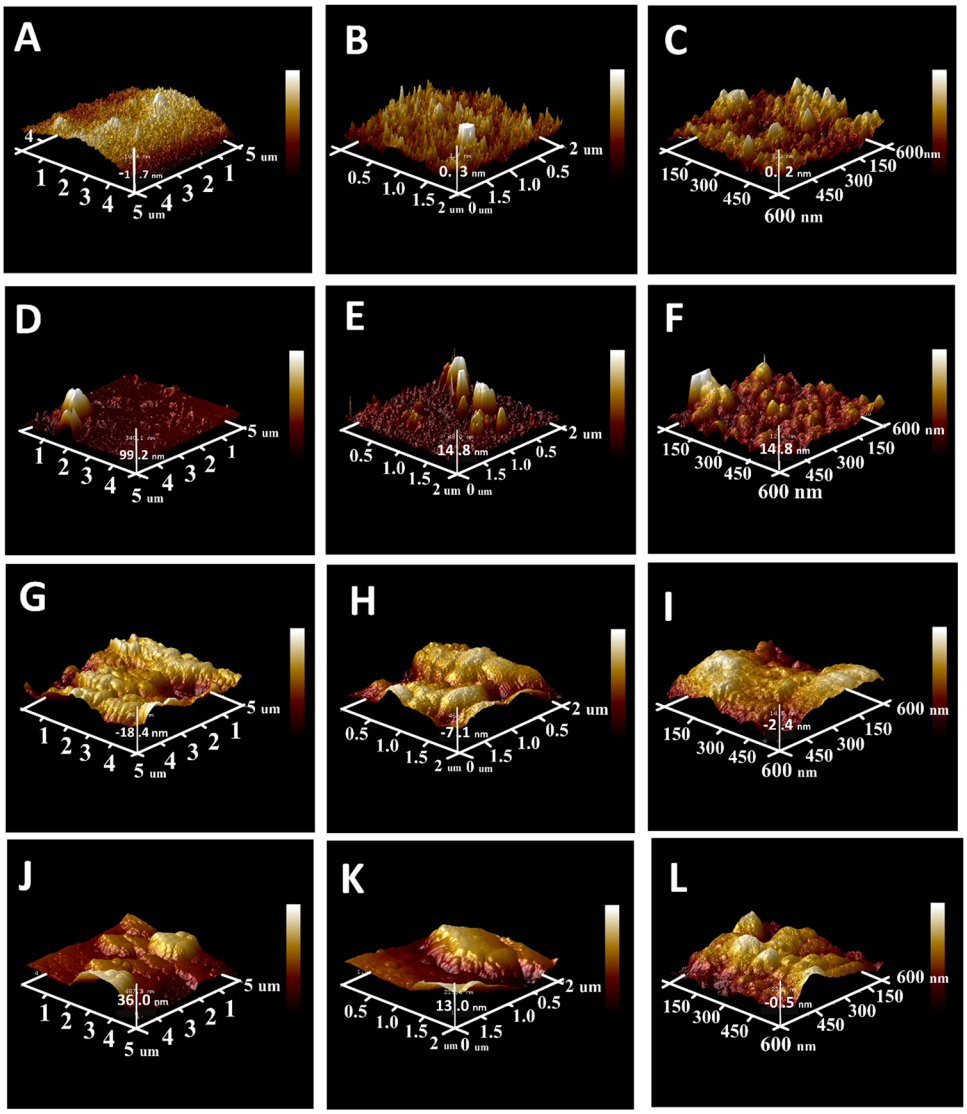

Fig. 7 3D AFM images of SF. (A)–(C) RNA (D)–(F) SF–RNA 1 h (G)–(I) and SF–RNA 6 h (J)–(L). For the first column, the scale bar is 1 μm, the second column is 400 nm, and the third column is 120 nm.

of absolute profile height values over the evaluation length; and maximum roughness depth (R_{max}), which denotes the largest among the successive maximum height values calculated over the evaluation length using nanoscale software. The findings revealed that the pristine SF exhibited the lowest surface roughness, while RNA and SF in the presence of RNA displayed higher surface roughness. With the increase in the time of incubation in PBS the surface roughness significantly increased (Fig. 9).

The changes in molecular interaction will lead to changes in the surface properties of the SF, and RNA, as visualized by AFM. The granular morphology of SF thin film was in agreement with the earlier reports.[39,40] The RNA and SF–RNA thin film showed bigger size granules. The bigger size granules due to the presence of RNA led to an increase in surface roughness, supporting the interaction of SF and RNA and their conformational changes. Increased surface roughness indicates a higher likelihood of contact, particularly van der Waals interactions, between the protein and the interacting molecule. This heightened roughness potentially leads to stronger interactions between the protein and the binding molecule.[41] These data were also in agreement with the contact angle measurement data.

ATR FTIR

To study the interactions between SF and RNA, FTIR spectra of SF, RNA–SF, and RNA were analyzed (Fig. 10). The presence of amide groups in silk protein manifested in distinctive vibration bands. The absorption peak around 1630–1650 cm^{-1} was attributed to the peptide backbone's amide I (C═O stretching). Bands around 1540–1520 cm^{-1} correspond to amide II (N–H bending), while bands at 1270–1230 cm^{-1} relate to amide III (C–N stretching), and 629 cm^{-1} to amide IV (Fig. 11A).[42] These characteristic absorbance peaks collectively signify the presence of a hydrogen-bonded NH group. The molecular conformation SF was

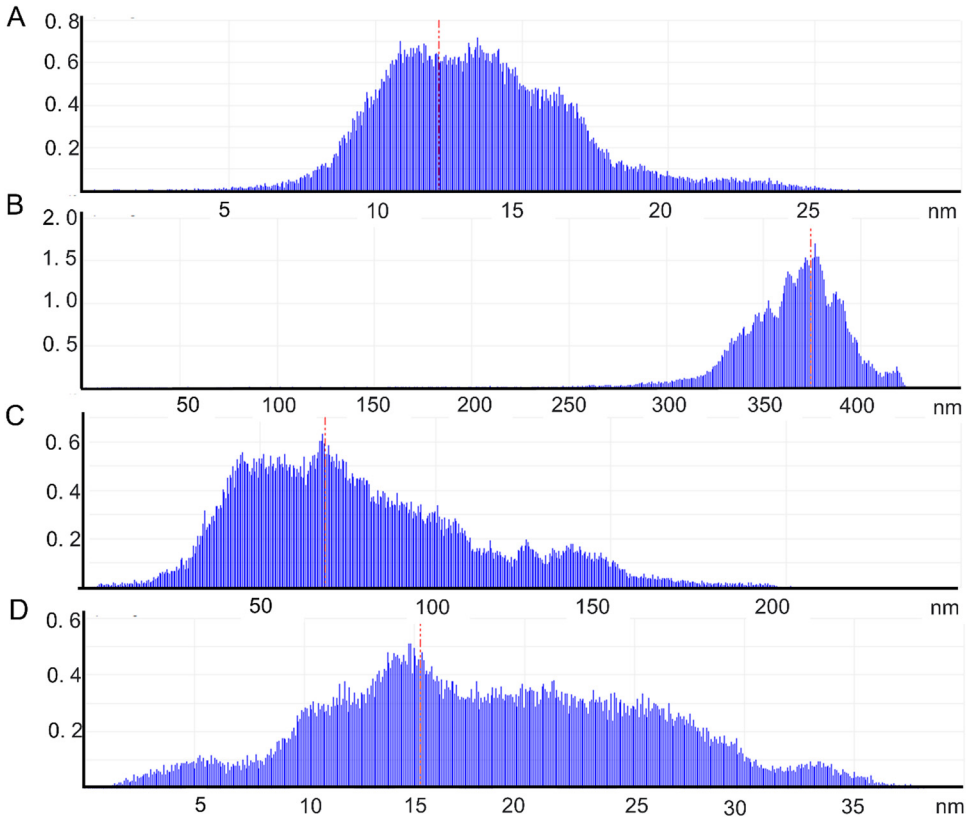

Fig. 8 Histogram of the height distribution function in AFM images of (A) SF, (B) RNA, (C) SF–RNA 1 h, and (D) SF–RNA 6 h. In all the figures, the *Y* axis is the % count and the *X* axis is depth histogram.

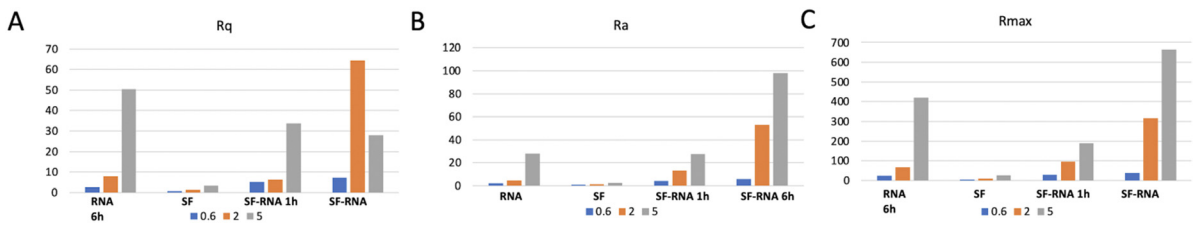

Fig. 9 Surface roughness measurement of SF, RNA, SF–RNA in 1 hour, and SF–RNA in 6 hours, by AFM. (A) RMS roughness (R_q), (B) roughness average (R_a), and (C) maximum roughness depth (R_{max}).

characterized by β-sheet absorption peaks at 1630, 1520, and 1240 cm^{-1}, random coil conformation absorption peaks at 1650, 1550, and 1230 cm^{-1}, and an α-helix absorption peak at 1655 cm^{-1}, along with turns at 1663–1696 cm^{-1}.[43] The FTIR spectrum of the RNA thin film exhibited multiple bands with varying intensities. In the 1500–1800 cm^{-1} region of FTIR, the peaks signify bonding in purine and pyrimidine bases within the strands. Peaks at 810 and 852 cm^{-1} specifically indicate ribose-phosphate vibrations, suggesting that the RNA under examination was of the A-RNA type. The bend stretching at 1244 represents the asymmetric stretch of PO_2.[44] Additionally, the peaks at 696, 754, and 624 cm^{-1} correspond to out-of-plane CH stretching, CN, and C–C out-of-plane vibrations, respectively. The FTIR peaks of RNA 624, 696, 754, 810, 852, 904, 1244, 1446, 1598, 1672 and 1741 stretched to 646, 719, 791, 887, 912, 944, 1267, 1467, 1639, 1687 and 1745 cm^{-1}, respectively, in SF–RNA, indicating strong interactions of RNA and SF. Furthermore, the impact of RNA on the secondary structure of SF was assessed by deconvoluting the 1600 to 1700 cm^{-1} region. The originally regenerated SF exhibited 11 peaks, representing various secondary protein structures, including side chains (1605–1615 cm^{-1}), β-sheets (1619–1628 and 1697–1703 cm^{-1}), random coil (1638–1655 cm^{-1}), α-helix (1656–1662 cm^{-1}), and turns (1663–1696 cm^{-1}), as previously reported.[45] In the presence of RNA, there was a notable increase in the percentage of β-sheet structure from 54 to 66, an augmentation in turns from 22 to 32, while the random coil decreased from 14 to 0.37, and α-helix decreased from 7 to null. These alterations signify the influence

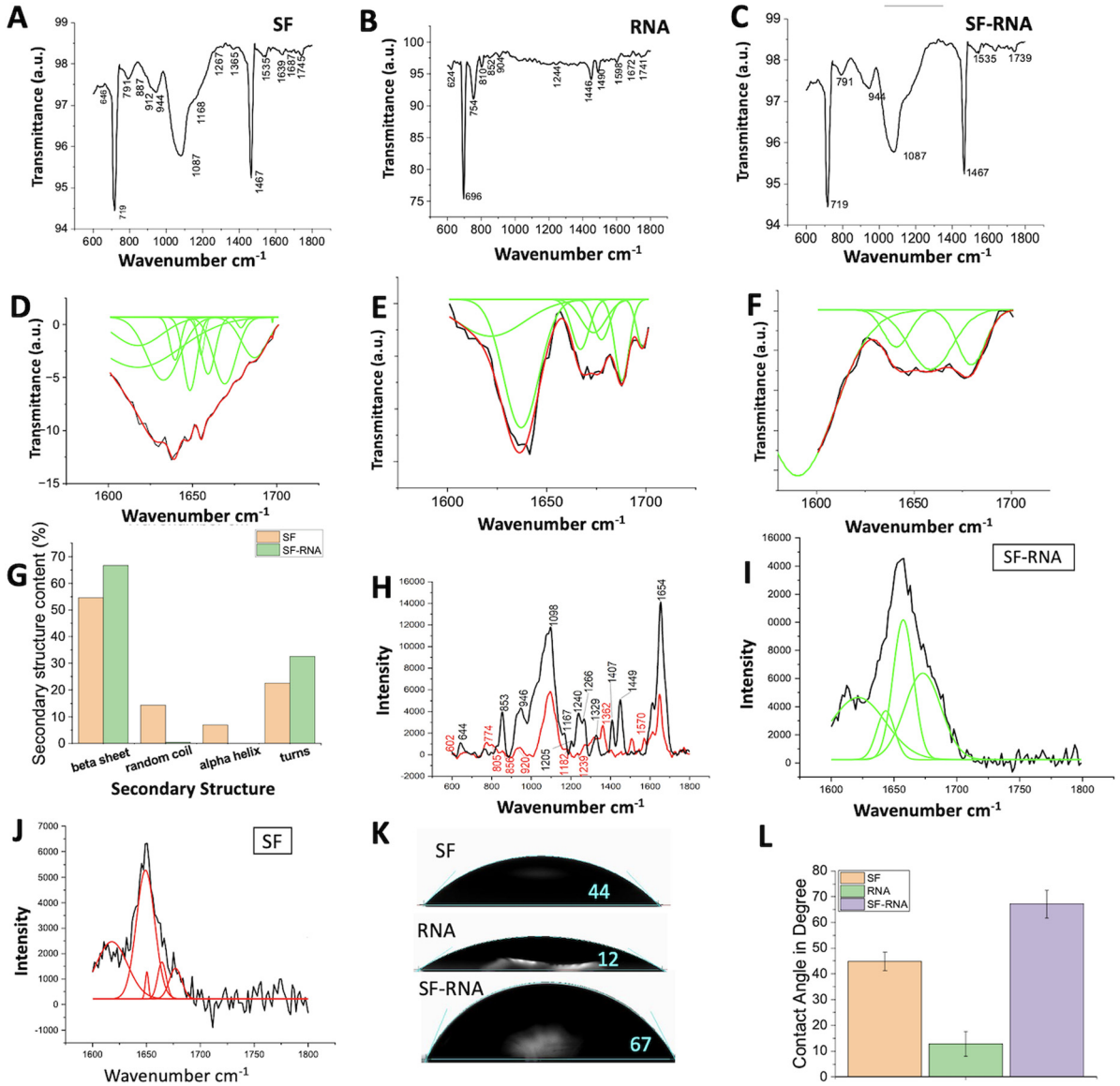

Fig. 10 FTIR spectra and contact angles of SF, RNA, and SF–RNA. FTIR spectra of (A) SF, (B) RNA, and (C) SF–RNA in the region of 1600–1800 cm^{-1}. Deconvolution of the 1600–1700 cm^{-1} region for (D) SF, (E) RNA, and (F) SF–RNA. (G) Percentage secondary structure in the amide-I region. (H) Raman spectra of SF and SF–RNA. (I) Deconvolution of the 1600–1800 cm^{-1} region of the Raman spectrum of SF. (J) Deconvolution of the 1600–1800 cm^{-1} region of the Raman spectrum of SF–RNA. (K) Representative contact angle, and (L) contact angle quantification for SF, RNA, and SF–RNA.

of RNA on the secondary structures of SF, resulting in a more pronounced presence of β-sheet structures and turns, while reducing the random coil and α-helix components.[46,47]

Raman spectroscopy

To find complementary peaks, Raman spectroscopy was performed on the thin film of SF and SF–RNA (Fig. 10H–J). In the Raman spectra of SF (Fig. 10H), the presence of peaks at 1612–1698 cm^{-1} is related to the amide I band, peaks at 1500–1570 peaks cm^{-1} are related to amide II, peaks at 1205–1276 cm^{-1} correspond to amide III, and the peak at 644 cm^{-1} is due to amide IV.[48,49] The presence of peaks at 1276, 1233, and 1668 cm^{-1} suggests the presence of β-sheet structures in SF, and those at 946 and 1654 cm^{-1} indicate the presence of α-helixes, and peaks at 1698 and 1684 cm^{-1} represent β-turns.[49,50] The presence of other peaks, such as those at 1098 cm^{-1} indicating C–C stretching vibration bands, 1752 cm^{-1} indicating C=O bonds, and 1167 cm^{-1} indicating C–N bonds, provides vital information on the complex chemical environment and hydrogen bonding in SF.

Moreover, the existence of shared peaks at 774, 853, 946, 1098, 1512, 1614, and 1654 cm^{-1} and specific peaks for RNA at 602, 805, 866, 991, 1181, 1362, 1570 and 1771 cm^{-1} in the SF–RNA Raman spectra highlights the intricate chemical combination and the resulting functional effects of RNA encapsulation. The peak at 602 cm^{-1} corresponds to ribose sugar, those at 856 and 920 cm^{-1} correspond to ribose phosphate stretching, that at

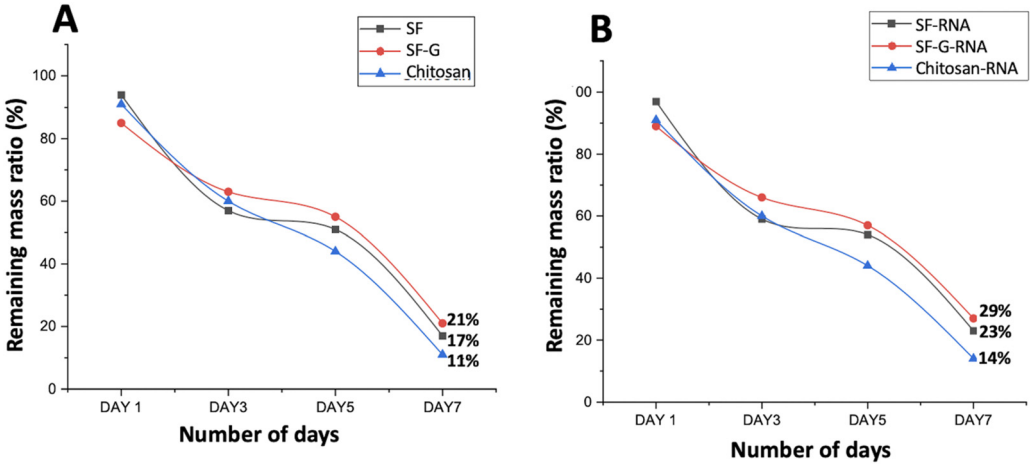

Fig. 11 Degradation study of the control and RNA-loaded hydrogel, (A) control hydrogels and (B) RNA-loaded hydrogels.

1239 cm^{-1} is due to asymmetric PO_2, and peaks from 1182–1570 cm^{-1} represent stretching vibrations for adenine–uracil–guanine–cytosine in the RNA.[51] The shifts in peaks at 1233, 1269, 1322, 1363, 1455, 1771, and 1405 cm^{-1} in SF RNA as compared to RNA, indicate strong chemical interactions between the SF–RNA complex (Fig. 10H). These changes are likely caused by hydrogen bonds, van der Waals contacts, and electrostatic interactions between SF and RNA molecules. These interactions eventually help to stabilize the β-sheet structures within the SF–RNA complex. From the deconvolution of Raman spectra (Fig. 10I and J) the increase in data β-sheet structure and β-turns validate the findings of FTIR.[52]

Contact angle

Contact angle measurements revealed the hydrophilic nature of SF, RNA, and SF–RNA. RNA exhibited the highest hydrophilicity with a contact angle of 12, followed by SF with a contact angle of 44, and SF–RNA with a contact angle of 67. The interaction of SF–RNA led to the exposure of more hydrophobic groups, resulting in increased hydrophobicity, as illustrated in Fig. 10K and L. This finding is consistent with the AFM data.

Degradation study between the control and RNA

The results indicate that the experimental group had a reduced rate of deterioration in comparison to the control group (Fig. 11). The remaining mass ratios at the end of day 7 for SF–RNA and SF–G–RNA films were approximately 6% and 8% greater than that of the control group. Furthermore, the difference in mass ratio between the control and experimental groups for chitosan films was approximately 3% greater after day 7. The results demonstrate that the experimental group, namely the films containing RNA, showed a notable decrease in degradation rate compared to the control group. Thus, our investigation confirms the idea that the inclusion of RNA in silk fibroin and silk fibroin gelatin films, as well as chitosan films, successfully reduces deterioration within a seven-day timeframe.

Materials and methods

Cell culture and RNA isolation

For the rat-derived TVA-BMSCs cell line (kindly provided by Prof. Amitabha Bandopadhyay, IIT Kanpur), passages 4–6, were expanded at 80% confluency in culture medium comprising alpha modified Eagle's medium (Gibco) supplemented with 15% fetal bovine serum (Gibco), and 1% penicillin/streptomycin (Gibco).[53] Total RNA was obtained using the RNeasy Mini Kit (Qiagen) according to the manufacturer's protocol.[54]

Preparation of silk fibroin (SF) solution

Bombyx mori cocoons were kindly provided by Central Silk Technological Research Institute (Central Silk Board), Bangalore, Ministry of Textiles, Government of India. Briefly, 5 g of silk cocoons were chopped into small pieces and boiled twice for about 20 min in 0.02 M Na_2CO_3 to remove sericin.[55,56] The fibres were dried overnight and dissolved in 9.3 M LiBr solution for 4 h at 60 °C, resulting in 15% w/v of aqueous silk fibroin solution. This resultant fibroin solution was dialyzed against deionized water using the Slide-a-Lyzer dialysis cassette at RT for 48 h for the removal of lithium bromide, resulting in 5% w/v of silk fibroin aqueous solution.

Fabrication of SF and gelatin (Gel)

To prepare the SF–Gel hydrogel solution, ethanol-sterilized gelatin powder (6% w/v) was added to autoclaved SF solution (5% w/v).[17] The mixture was then incubated at 37 °C for 1 hour. Enzymatic crosslinking was achieved by adding 800 units of mushroom tyrosinase to the solution, followed by thorough mixing. The solution was mixed properly and the thin film was cast from 150 μL of solution in 24 well-plate sterile cell culture plates.

RNA polymer interaction study

The RNA polymer was examined by incubating 2 μL of RNA with 50 μL of 2% Gel, 2% SF, and a 1 : 1 ratio of 2% Gel and SF mixture. The incubation took place at room temperature for

30 minutes. Subsequently, 7 μL of each RNA sample was loaded onto a 1% agarose gel in tris-borate-EDTA (TBE) buffer, pH 8.3 for gel electrophoresis analysis.

Tyramine modification for gelatin (Gel–TA)

Gel–TA derivatives were synthesized using a carbodiimide-mediated reaction according to a previously described method.[26] Here, 2% (w/v) gelatin solutions were prepared in 0.05 M 2-(*N*-morpholino) ethane sulfonic acid (MES) buffer at pH 6.0. These solutions were then mixed with tyramine hydrochloride (500 mg per 1 g protein), 1-ethyl-3-(-3-dimethylaminopropyl) carbodiimide hydrochloride (EDC) (184 mg per 1 g protein), and *N*-hydroxysuccinimide (NHS) (57 mg per 1 g protein). The reaction took place under stirring at room temperature (24 °C) for 18 hours. To remove any unreacted components and by-products, the solutions were dialyzed against distilled water using tubing with a molecular weight cutoff (MWCO) of 3.5 kDa. This dialysis process involved six changes of water over three days, continuing until the absorbance at 275 nm was undetectable in the filter solution, as determined by a UV spectrophotometer. Finally, the Gel–TA solution was stored at 4 °C for further use.[57]

Characterization of tyramine modification

The absorbance spectra ranging from 250 nm to 350 nm were recorded for solutions containing 1% Gel, as well as Gel–TA solution. The percentage of tyramine modification was determined by comparing the absorbance values to a tyramine standard curve prepared in distilled water.[57]

Zeta potential measurement

To investigate the tyramine modification and polymer–RNA interaction, the zeta potential of various samples was measured. Solutions of 2% Gel, Gel–RNA, Gel–TA, Gel–TA–RNA, SF, SF–RNA, as well as 0.1% Chi and Chi–RNA, were prepared in distilled water. The zeta potential measurements were performed using the Malvern Zeta sizer Nano ZS90 instrument (Malvern Panalytical Ltd, UK). The analysis took place at a temperature of 25 °C, employing a scattering angle of 90°.[54,58] For each sample, the zeta potential analysis was conducted three times to ensure accuracy and reliability. The average zeta potential value was calculated based on three different samples synthesized under the same conditions.

The effects of H_2O_2, HRP, and tyrosinase on RNA stability

The effects of H_2O_2, HRP, and tyrosinase on RNA stability were evaluated by incubating 7 ng of RNA in 3 mM H_2O_2, 3 units of HRP, 3 mM H_2O_2 + 3 units of HRP, and 800 units of tyrosinase for 30 minutes. The total RNA was measured by NANO Drop (Thermo Fisher Scientific) by measuring the absorbance at the 260/280 ratio.

Fabrication of Gel–TA hydrogel

The Gel–TA polymer solution, with a standardized concentration of 2% (w/v), was utilized to ensure the formation of stable thin films. To create the Gel–TA hydrogel, the solution was crosslinked using horseradish peroxidase (HRP) and hydrogen peroxide (H_2O_2).[24] The impact of HRP and H_2O_2 on stable thin film formation was investigated and standardized accordingly. When RNA is treated with H_2O_2, it can generate reactive species like hydroxyl radicals and peroxyl radicals. These radicals further interact with RNA, causing oxidation or strand breaks, which can destabilize the RNA within the hydrogel. For the standardization of HRP concentration (ranging from 1 to 5 units), the Gel–TA concentration (2% w/v) and H_2O_2 concentration (3 mM) were kept constant. This systematic approach allowed for the determination of the optimal HRP concentration required for the formation of stable thin films. Similarly, the standardization of the H_2O_2 concentration (ranging from 1 to 4 mM) was achieved by maintaining a constant Gel–TA concentration (2% w/v) and HRP concentration (3 units). This ensured the identification of the ideal H_2O_2 concentration for stable thin film formation. For the casting of thin films, approximately 150 μL of the Gel–TA solution was used. This volume was chosen to ensure the appropriate thickness of the resulting thin film hydrogel.

Fabrication of chitosan hydrogel

Chi hydrogel was made using a 2% chitosan low-viscosity solution in 0.5% acetic acid.[59] To fabricate chitosan-based hydrogel thin films, TPP was incorporated as a cross-linker. To standardize the TPP concentration (ranging from 0% to 1%), we maintained a constant volume of 0.5 mL of TPP. Similarly, to standardize the TPP volume (ranging from 0 mL to 1 mL), we kept the TPP concentration at 1%. This systematic approach allowed us to explore the influence of both TPP concentration and volume on the hydrogel formation process. For the casting of thin films, approximately 150 μL of the chitosan solution was utilized. This ensured an optimal thickness for the resulting thin film hydrogel.

RNA-loaded hydrogel fabrication

The Gel–TA–RNA hydrogel was prepared by combining 500 μL of a 2% Gel–TA solution with 5 μL of RNA. Subsequently, 3 mM H_2O_2 and 3 units of HRP were added to the mixture, quickly mixed, and a thin film was cast using 150 μL of the solution. For the SF–Gel–TA–RNA hydrogel, 500 μL of a mixture containing 5% SF and 2% Gel–TA (in a 1 : 1 ratio) was combined with 5 μL of RNA. Following this, 3 mM H_2O_2 and 3 units of HRP were added, the mixture was quickly mixed, and a thin film was cast using 150 μL of the solution. In the case of the SF–RNA hydrogel, a 5% SF solution (500 μL) was mixed with 5 μL of RNA and crosslinked using 800 units of mushroom tyrosinase. The resulting solution was mixed, and a thin film was cast using 150 μL of the mixture. For the Chi–RNA hydrogel, 2% chitosan in a 0.5% acetic acid solution was mixed with 5 μL of RNA. The thin film was then cast using 150 μL of the solution and crosslinked with 1% TPP (1 mL).

Release kinetics and stability study

To evaluate the release kinetics of the thin film hydrogels, 150 μL of solution from each experimental group was cast, followed by immersion in 300 μL of PBS (pH 7.4). On days 1, 2,

and 3, approximately 50 μL of the released solution was collected for analysis. As a control, hydrogels without RNA were included, and the absorbance of the respective mRNA groups was subtracted from the collected solution, the RNA was measured using a NANO Drop Spectrophotometer. For the stability study, 7 μL of the collected released solution from the release kinetics experiment was loaded onto a 1% agarose gel in RBE buffer. This gel electrophoresis analysis allowed for the assessment of RNA stability within the hydrogel system.

Apparent RNA measurement to evaluate RNA–polymer interaction

The RNA detected during the release kinetics was higher than the initially loaded amount of RNA. This intriguing result prompted us to investigate the interaction between the polymer and RNA more closely. To conduct this investigation, we prepared a solution containing 40 ng μL^{-1} of RNA mixed with 10 μL of different solutions: PBS, 0.1% chitosan, 1% Gel, 1% Gel–TA, 1% Gel–TA + 1% SF, or 1% SF. Thorough mixing was performed to ensure proper dispersion of RNA and polymers in each solution. Quantification of RNA content was performed using the NANO Drop. All experiments were conducted in triplicate to ensure the reliability and consistency of our findings.

Stability of RNA in the presence of RNAse

To determine RNA stability with polymers in the presence of RNAse, we prepared a solution containing 27 ng μL^{-1} of RNA mixed with 10 μL of different solutions: PBS, 0.1% chitosan, 1% Gel, 1% SF, and 1% GEL + 1% SF or 1% Gel–TA + 1% SF. The mixtures were incubated in the presence or absence of 2 μL of RNAse (1 mg mL^{-1} stock)/RNAse-free water in the control. Thorough mixing was performed to ensure proper dispersion of RNA and polymers in each solution. Quantification of RNA content was performed using the NANO Drop technique. All experiments were conducted in triplicate to ensure the reliability and consistency of our findings.

Molecular docking

The molecular docking process employed the HDOCK server and involved the retrieval of PDB structures from the RCSB Protein Data Bank, including 28S rRNA from *Rattus norvegicus* (PDB ID: 430d), the N-terminal of SF from *Bombyx mori* (PDB ID: 3ua0), and the collagen triple helix (PDB ID: 1k6f). Additionally, the SDF structure of chitosan was sourced from PubChem. FASTA files for 18S rRNA (URS00022B2FF1 rRNA), 5.8S rRNA (URS00006A440B rRNA), 5S rRNA (URS000068F315 rRNA), tRNA-ALA (URS000073E85F tRNA), tRNA-Leu (URS000015C515 tRNA), and tRNA-GLN (URS000059E5F0 tRNA) were obtained from RNA central, while beta actin mRNA (NM_031144.3), GAPDH mRNA (NM_017008.4), and Nanog (AB275459.1) were downloaded from NCBI.

To facilitate compatibility with the docking process, the SDF file for chitosan and FASTA sequences was converted into PDB format using the Openbabel software. During docking, the macromolecules SF, collagen, or chitosan were designated as the receptors, while the respective RNA molecules served as ligands. The HDOCK server executed global docking, involving the exploration of potential binding modes through an FFT-based search method. Subsequently, these binding modes underwent evaluation using an intrinsic scoring function tailored specifically for protein–RNA interactions.[60] The docked structures were visualized using PyMOL.

Atomic force microscopy (AFM)

AFM imaging was performed on a Bruker Dimension Icon in peak force tapping mode, using MSNL-10 (Bruker) probes. A thin film was cast using 40 μL of SF or SF–RNA (a mixture of 5% of SF of 40 ng μL^{-1} RNA) on a glass slide and allowed to dry followed by fixation in 4% PFA in PBS. The AFM scan rate was 0.996 Hz and with scanning sizes of 5, 2, and 0.6 μm. All images were treated with the ''flatten'' function using Nanoscope 2 software. The depth analysis and surface roughness were analyzed using the Nanoscope 2 software.

Attenuated total reflectance-Fourier transform infrared spectroscopy (ATR-FTIR)

ATR-FTIR was conducted in absorption mode using a PerkinElmer instrument (Spectrum BX Series, MA, USA). The spectra were acquired within the region of 600–1800 cm^{-1} using a deuterated triglycine sulfate IR detector. Each sample underwent 64 scans at a resolution of 4 cm^{-1} and was subsequently deconvoluted using OriginPro 2023b (Origin Lab Corporation, Northampton, MA, USA). Prior to deconvolution, baseline correction and area normalization were performed.[56]

Raman spectroscopy

We acquired Raman spectra of the SF and SF–RNA utilizing a confocal laser dispersion micro-Raman spectrometer (inVia reflex, UK) equipped with a 538 nm diode laser and integrated with the FTIR IlluminatIR II module. All Raman measurements were conducted at a magnification of 10×. The samples were prepared by casting a thin film by placing 40 μL of SF or SF–RNA (a mixture of 5% of SF of 40 ng μL^{-1} RNA) on a glass slide and allowing it to dry, followed by fixation in 4% PFA in PBS. The measurements were captured at five randomly selected points per sample, each with an integration time of 10 seconds, and subsequently deconvoluted using OriginPro 2023b (Origin Lab Corporation, Northampton, MA, USA). Before deconvolution, baseline correction and area normalization were performed.

Contact angle measurement using goniometry

Goniometry was employed for measuring the static apparent contact angles of SF, SF–RNA, and RNA as reported earlier with a slight modification. A 5 μL deionized water droplet was placed on each sample using the KRUSS DSA-100 Drop Shape Analyzer. To prepare the samples for contact angle measurement, thin films of SF, SF–RNA, and RNA were cast onto glass slides using a 100 μL solution, and the films were allowed to dry, forming thin films. All the experiments were done in triplicate.

Degradation study between the control and RNA

The degradation study, done over a period of seven days, compared the rates of degradation between a control group consisting of films made of silk fibroin, silk fibroin gelatin, and chitosan, and an experimental group consisting of films made of SF–RNA, SF–G–RNA, and chitosan–RNA. Under sterile environments, a total of 24 films were distributed evenly into Petri dishes, with 12 films assigned to each group. The films were categorized into four subgroups, which corresponded to day 1, day 3, day 5, and day 7 for both the control and experimental groups. After the casting process, the films were freeze-dried to remove moisture and then kept at a temperature of −20 °C for weight measurements on specific days.

Statistics

All quantitative results were expressed as mean ± standard deviation. Statistical analyses were performed using Student's *t*-test, or one-way ANOVA test based on the requirement. All values of $P < 0.05$ were regarded to be statistically significant.

Conclusions

Our findings highlight the potential of hydrogel-based systems, specifically the SF–Gel composites, for effective RNA delivery. The incorporation of silk fibroin and the modification of gelatin improved the stability, protection, and affinity of the hydrogel for RNA. The gel electrophoresis and zeta potential data provided valuable insights into the behavior of RNA within the hydrogel systems. Gel electrophoresis analysis revealed that Gel alone was insufficient to protect the RNA from degradation, whereas the SF and SF–Gel composites formed complexes with the RNA, indicating enhanced stability and protection. Similarly, zeta potential measurements indicated that the SF–RNA complex exhibited increased exposure of amino groups on the outer surface imparting a reduction in the negative value of the zeta potential as compared to the SF alone, highlighting the interaction and stabilization of RNA by silk fibroin.

To enhance the protection and delivery of negatively charged mRNA, we employed a modification strategy, neutralizing gelatin's free carboxyl groups with tyramine molecules. The successful tyramine modification, confirmed by a positive zeta potential, resulted in the reduction of negatively charged carboxyl groups. The experimental and molecular modelling indicated that the RNA has strong interaction with SF as compared to chitosan, followed by collagen, evidenced by the larger number of hydrogen bonds and lower root mean square deviation (RMSD) values in most cases. Specific residues involved in these interactions were identified, highlighting the importance of polar amino acids in SF, Gly and Pro in collagen, and donor–acceptor pairs in chitosan. The 3D structure of AFM images emphasized the uniformity of grains in SF, contrasting with the nonuniform and larger grains in RNA and SF–RNA. The increase in grain size and surface roughness with prolonged incubation in PBS indicated significant changes in molecular interactions and structural properties. The observed increase in surface roughness supports the notion that interactions with RNA induce conformational changes in SF molecules, exposing different regions and potentially strengthening the interactions. Upon interaction with SF, the peaks in the FTIR and Raman spectra of RNA shifted, indicating a strong interaction between RNA and SF. Deconvolution of the secondary structure region revealed significant changes in the SF secondary structure in the presence of RNA, with increased β-sheet structures and turns, and decreased random coil and α-helix components. These findings underscore the profound impact of RNA on the molecular conformation of SF, shedding light on the intricate interplay between these biomolecules and offering valuable insights for applications in biotechnology and material science. The contact angle measurements revealed that RNA demonstrated the highest hydrophilicity, followed by SF, and SF–RNA. This sequence suggests the exposure of more hydrophobic groups in SF–RNA, leading to an overall increase in hydrophobicity. Remarkably, these results align with the findings from AFM and molecular modeling data, providing a consistent picture of the changes in surface properties and intermolecular interactions between SF and RNA.

These advancements have significant implications for the development of RNA-based therapies, where effective delivery and protection are critical for therapeutic success.

Conflicts of interest

The authors declare that they have no known competing financial interests or personal relationships that could have appeared to influence the work reported in this paper.

Acknowledgements

We are grateful to the Department of Biotechnology (DBT) India for the BIRAC (Biotechnology Industry Research Council) funding (Project number: BIRAC/SIIC0273/BIG-16/20).

References

1 K. S. Corbett, D. K. Edwards, S. R. Leist, O. M. Abiona, S. Boyoglu-Barnum, R. A. Gillespie, S. Himansu, A. Schäfer, C. T. Ziwawo, A. T. DiPiazza, K. H. Dinnon, S. M. Elbashir, C. A. Shaw, A. Woods, E. J. Fritch, D. R. Martinez, K. W. Bock, M. Minai, B. M. Nagata, G. B. Hutchinson, K. Wu, C. Henry, K. Bahl, D. Garcia-Dominguez, L. Ma, I. Renzi, W.-P. Kong, S. D. Schmidt, L. Wang, Y. Zhang, E. Phung, L. A. Chang, R. J. Loomis, N. E. Altaras, E. Narayanan, M. Metkar, V. Presnyak, C. Liu, M. K. Louder, W. Shi, K. Leung, E. S. Yang, A. West, K. L. Gully, L. J. Stevens, N. Wang, D. Wrapp, N. A. Doria-Rose, G. Stewart-Jones, H. Bennett, G. S. Alvarado, M. C. Nason, T. J. Ruckwardt, J. S. McLellan, M. R. Denison, J. D. Chappell, I. N. Moore, K. M. Morabito, J. R. Mascola, R. S. Baric, A. Carfi and B. S. Graham, *Nature*, 2020, **586**, 567–571.

2 N. Pardi, M. J. Hogan, R. S. Pelc, H. Muramatsu, H. Andersen, C. R. DeMaso, K. A. Dowd, L. L. Sutherland, R. M. Scearce and R. Parks, *Nature*, 2017, **543**, 248–251.
3 M. S. Kormann, G. Hasenpusch, M. K. Aneja, G. Nica, A. W. Flemmer, S. Herber-Jonat, M. Huppmann, L. E. Mays, M. Illenyi and A. Schams, *Nat. Biotechnol.*, 2011, **29**, 154–157.
4 R. Zhong, S. Talebian, B. B. Mendes, G. Wallace, R. Langer, J. Conde and J. Shi, *Nat. Mater.*, 2023, **22**(7), 818–831.
5 L. L. Wang, J. N. Sloand, A. C. Gaffey, C. M. Venkataraman, Z. Wang, A. Trubelja, D. A. Hammer, P. Atluri and J. A. Burdick, *Biomacromolecules*, 2017, **18**, 77–86.
6 S. F. Dowdy, *Nat. Biotechnol.*, 2017, **35**, 222–229.
7 Y. Yan, X.-Y. Liu, A. Lu, X.-Y. Wang, L.-X. Jiang and J.-C. Wang, *J. Controlled Release*, 2022, **342**, 241–279.
8 H. Steinle, T. M. Ionescu, S. Schenk, S. Golombek, S. J. Kunnakattu, M. T. Özbek, C. Schlensak, H. P. Wendel and M. Avci-Adali, *Int. J. Mol. Sci.*, 2018, 19.
9 B. Maity, H. Moorthy and T. Govindaraju, *ACS Appl. Mater. Interfaces*, 2023, **15**, 49953–49963.
10 B. Maity, S. Samanta, S. Sarkar, S. Alam and T. Govindaraju, *ACS Appl. Bio Mater.*, 2020, **3**, 3544–3552.
11 L. P. Datta, S. Manchineella and T. Govindaraju, *Biomaterials*, 2020, **230**, 119633.
12 S. Das, F. Pati, Y. J. Choi, G. Rijal, J. H. Shim, S. W. Kim, A. R. Ray, D. W. Cho and S. Ghosh, *Acta Biomater.*, 2015, **11**, 233–246.
13 S. Murab, J. Samal, A. Shrivastava, A. R. Ray, A. Pandit and S. Ghosh, *Biomaterials*, 2015, **55**, 64–83.
14 E. M. Pritchard and D. L. Kaplan, *Expert Opin. Drug Delivery*, 2011, **8**, 797–811.
15 L. L. Wang and J. A. Burdick, *Adv. Healthcare Mater.*, 2017, 6.
16 S. Das, F. Pati, Y.-J. Choi, G. Rijal, J.-H. Shim, S. W. Kim, A. R. Ray, D.-W. Cho and S. Ghosh, *Acta Biomater.*, 2015, **11**, 233–246.
17 S. Das, F. Pati, S. Chameettachal, S. Pahwa, A. R. Ray, S. Dhara and S. Ghosh, *Biomacromolecules*, 2013, **14**, 311–321.
18 C. Guo, C. Li and D. L. Kaplan, *Biomacromolecules*, 2020, **21**, 1678–1686.
19 D. Trucco, A. Sharma, C. Manferdini, E. Gabusi, M. Petretta, G. Desando, L. Ricotti, J. Chakraborty, S. Ghosh and G. Lisignoli, *ACS Biomater. Sci. Eng.*, 2021, **7**, 3306–3320.
20 J. He, B. Yavuz, J. A. Kluge, A. B. Li, F. G. Omenetto and D. L. Kaplan, *ACS Biomater. Sci. Eng.*, 2018, **4**, 1708–1715.
21 L. Andrée, R. Oude Egberink, J. Dodemont, N. Hassani Besheli, F. Yang, R. Brock and S. C. G. Leeuwenburgh, *Nanomaterials*, 2022, 12.
22 J. A. Kluge, B. T. Kahn, J. E. Brown, F. G. Omenetto and D. L. Kaplan, *ACS Biomater. Sci. Eng.*, 2016, **2**, 595–605.
23 H. Ragelle, R. Riva, G. Vandermeulen, B. Naeye, V. Pourcelle, C. S. Le Duff, C. D'Haese, B. Nysten, K. Braeckmans, S. C. De Smedt, C. Jérôme and V. Préat, *J. Controlled Release*, 2014, **176**, 54–63.
24 Y. Y. Chun, Z. L. Yap, L. F. Seet, H. H. Chan, L. Z. Toh, S. W. L. Chu, Y. S. Lee, T. T. Wong and T. T. Y. Tan, *Sci. Rep.*, 2021, **11**, 1470.
25 R. Nyaruaba, W. Hong, X. Li, H. Yang and H. Wei, *Anal. Chem.*, 2022, **94**, 4522–4530.
26 O. Hasturk, K. E. Jordan, J. Choi and D. L. Kaplan, *Biomaterials*, 2020, **232**, 119720.
27 W. E. Rudzinski and T. M. Aminabhavi, *Int. J. Pharm.*, 2010, **399**, 1–11.
28 K. A. Howard, U. L. Rahbek, X. Liu, C. K. Damgaard, S. Z. Glud, M. Ø. Andersen, M. B. Hovgaard, A. Schmitz, J. R. Nyengaard and F. Besenbacher, *Mol. Ther.*, 2006, **14**, 476–484.
29 W. Zhang, H. Yang, X. Kong, S. Mohapatra, H. S. Juan-Vergara, G. Hellermann, S. Behera, R. Singam, R. F. Lockey and S. S. Mohapatra, *Nat. Med.*, 2005, **11**, 56–62.
30 J. Y. Pillé, H. Li, E. Blot, J. R. Bertrand, L. L. Pritchard, P. Opolon, A. Maksimenko, H. Lu, J. P. Vannier, J. Soria, C. Malvy and C. Soria, *Hum. Gene Ther.*, 2006, **17**, 1019–1026.
31 M. Karimi, P. Avci, M. Ahi, T. Gazori, M. R. Hamblin and H. Naderi-Manesh, *J. Nanopharm. Drug Delivery*, 2013, **1**, 266–278.
32 J. C. Fernandes, X. Qiu, F. M. Winnik, M. Benderdour, X. Zhang, K. Dai and Q. Shi, *Int. J. Nanomed.*, 2012, **7**, 5833–5845.
33 X. R. Shao, X. Q. Wei, X. Song, L. Y. Hao, X. X. Cai, Z. R. Zhang, Q. Peng and Y. F. Lin, *Cell Prolif.*, 2015, **48**, 465–474.
34 R. E. Hubbard and M. Kamran Haider, *Encyclopedia of Life Sciences*, 2010.
35 P. Prentø, *Biotech. Histochem.*, 2007, **82**, 199–200.
36 A. Avdoshin, V. Naumov, L. C. Ciacchi, S. Ignatov and S. Köppen, *Mater. Adv.*, 2023, **4**, 1113–1124.
37 N. Majumder, C. Roy, L. Doenges, I. Martin, A. Barbero and S. Ghosh, *ACS Appl. Mater. Interfaces*, 2024, **16**(8), 9925–9943.
38 N. Majumder, S. Seit, N. S. Bhabesh and S. Ghosh, *Adv. Healthcare Mater.*, 2024, 2303513.
39 F. Galeotti, A. Andicsova, F. Bertini and C. Botta, *J. Mater. Sci.*, 2013, **48**, 7004–7010.
40 J. H. Choi, M. Choi, T. Kang, T. S. Ho, S. H. Choi and K. M. Byun, *Biosensors*, 2021, **11**(11), 441.
41 A. Banerji and C. Navare, *J. Mol. Recognit.*, 2013, **26**, 201–214.
42 S.-W. Ha, A. E. Tonelli and S. M. Hudson, *Biomacromolecules*, 2005, **6**, 1722–1731.
43 H. Zhang, L. L. Li, F. Y. Dai, H. H. Zhang, B. Ni, W. Zhou, X. Yang and Y. Z. Wu, *J. Transl. Med.*, 2012, **10**, 117.
44 P. Routh, A. Garai and A. K. Nandi, *Phys. Chem. Chem. Phys.*, 2011, **13**, 13670–13682.
45 B. D. Lawrence, F. Omenetto, K. Chui and D. L. Kaplan, *J. Mater. Sci.*, 2008, **43**, 6967–6985.
46 S. Midha, R. Tripathi, H. Geng, P. D. Lee and S. Ghosh, *Mater. Sci. Eng., C*, 2016, **8**, 663–674.
47 S. Midha, S. Chawla, J. Chakraborty, S. Chameettachal and S. Ghosh, *ACS Biomater. Sci. Eng.*, 2018, **4**, 595–607.
48 P. Monti, P. Taddei, G. Freddi, T. Asakura and M. Tsukada, *J. Raman Spectrosc.*, 2001, **32**, 103–107.
49 Q. Wang, P. McArdle, S. L. Wang, R. L. Wilmington, Z. Xing, A. Greenwood, M. L. Cotten, M. M. Qazilbash and H. C. Schniepp, *Nat. Commun.*, 2022, **13**, 4329.
50 S. Zheng, G. Li, W. Yao and T. Yu, *Appl. Spectrosc.*, 1989, **43**, 1269–1272.

51 A. J. Hobro, M. Rouhi, E. W. Blanch and G. L. Conn, *Nucleic Acids Res.*, 2007, **35**, 1169–1177.
52 S. Murab and S. Ghosh, *Biomed. Mater.*, 2016, **11** 065005.
53 S. Midha, S. Kumar, A. Sharma, K. Kaur, X. Shi, P. Naruphontjirakul, J. R. Jones and S. Ghosh, *Biomed. Mater.*, 2018, **13**, 055012.
54 J. Chakraborty, N. Majumder, A. Sharma, S. Prasad and S. Ghosh, *Bioprinting*, 2022, **28**, e00232.
55 S. Chawla, A. Kumar, P. Admane, A. Bandyopadhyay and S. Ghosh, *Bioprinting*, 2017, **7**, 1–13.
56 P. Dubey, P. K. Chowdhury and S. Ghosh, *Biochim. Biophys. Acta, Proteins Proteomics*, 2019, **1867**, 416–425.
57 S. Sakai, K. Hirose, K. Taguchi, Y. Ogushi and K. Kawakami, *Biomaterials*, 2009, **30**, 3371–3377.
58 B. Mahaling and D. S. Katti, *Nanomedicine*, 2016, **12**, 2149–2160.
59 K. C. McCullough, I. Bassi, P. Milona, R. Suter, L. Thomann-Harwood, P. Englezou, T. Démoulins and N. Ruggli, *Mol. Ther.--Nucleic Acids*, 2014, 3.
60 Y. Yan, H. Tao, J. He and S.-Y. Huang, *Nat. Protoc.*, 2020, **15**, 1829–1852.

